Composites: Part B 62 (2014) 159–166

Contents lists available at ScienceDirect

Composites: Part B

journal homepage: www.elsevier.com/locate/compositesb

Mechanical characteristics and strengthening effectiveness of random-chopped FRP composites containing air voids

B.J. Yang [a], S.K. Ha [a], S.H. Pyo [b], H.K. Lee [a,*]

[a] Department of Civil and Environmental Engineering, Korea Advance Institute of Science and Technology (KAIST), 291 Daehak-ro, Yuseong-gu, Daejeon 305-701, Republic of Korea
[b] Department of Civil and Environmental Engineering, University of Michigan, Ann Arbor, MI 48109-2125, USA

ARTICLE INFO

Article history:
Received 30 November 2013
Received in revised form 28 January 2014
Accepted 14 February 2014
Available online 6 March 2014

Keywords:
A. Polymer–matrix composites (PMCs)
B. Porosity
C. Numerical analysis
D. Mechanical testing

ABSTRACT

In random-chopped fiber-reinforced polymer (FRP) composites used as a retrofit material, a high volume fraction of voids is inevitable due to the manufacturing characteristics. In this paper, the mechanical characteristics and strengthening effectiveness of random-chopped FRP composites containing air porosity are investigated through experiments and numerical analysis. Coupon-shaped specimens with various material compositions were manufactured to examine the uniaxial tensile performance, and the air voids in the composites were measured by a microscope camera. In order to predict the overall performance of the composites, a micromechanical formulation that accounts for porosity was newly developed. The derived model was incorporated into a finite element (FE) code, and the model parameters were estimated by comparing uniaxial tensile test results for various systems of random-chopped FRP composites. In addition, concrete beams strengthened with the composites were produced to evaluate their load-carrying capacity. The FE predictions of the composite structures were then compared with experimental data to verify the predictive capability of the proposed numerical framework.

1. Introduction

Composites are artificial multi-phase systems with enhanced properties such as high levels of strength and rigidity and good thermal properties [1–4]. Fiber-reinforced polymer (FRP) composites are a broad category of composite materials that are made from an environmentally resistant polymer resin matrix and stiff reinforcing fibers [5–8]. Recently, in the engineering field, requirements for reliable rehabilitation strategies for existing structures have increased due to environmental considerations and structural deterioration [9]. The conventional retrofitting and rehabilitation methods accompany several drawbacks, including difficulties related to the handling of heavy materials, the deterioration of bonds, and corrosion [10]. In light of these problems, 2D randomly oriented chopped fiber-reinforced composites manufactured by a spray lay-up process are being considered as a candidate retrofit material on the basis of their competitive advantages, including low cost, versatility, and easy applicability [11,12].

The application of random-chopped sprayed FRP composites, however, is impeded by the presence of voids, which are primarily formed by entrapped air in the composites and various volatile substances dissolved in the resin matrix [13–15]. Inadequate curing temperatures and processes are also responsible for the formation of voids [16]. For the commercial manufacturing processes of random-chopped FRP composites, the process pressure and temperature of injection and compression molding are as follows: 75–150 MPa and 140 °C for injection molding and 5–15 MPa and 130–150 °C for compression molding processes [17]. Regarding other parameters, random-chopped FRP composites as a retrofit material are manufactured under field application conditions such as very low compaction pressure by manual roll-out work and ambient curing temperature in air [18]. The presence of air voids in random chopped FRP composites is inevitable due to the aforementioned application conditions [17]. To reliably and accurately predict the behavior and performance of the retrofit material, air voids in the composites should be considered.

In this paper, the mechanical characteristics and strengthening effectiveness of the random chopped fiber-reinforced polymer (FRP) composites are investigated. First, FRP composites with various lengths and volume fractions of random-chopped fibers were manufactured by a spray lay-up process, and they were produced as coupon-shaped specimens for uniaxial tensile evaluations. The porosity contents in the composites were evaluated by a microscope image analysis, and measurements were applied to the proposed model for a more accurate estimation. In addition, a

* Corresponding author. Tel.: +82 42 350 3623; fax: +82 42 350 3610.
E-mail address: leeh@kaist.ac.kr (H.K. Lee).

http://dx.doi.org/10.1016/j.compositesb.2014.02.015
1359-8368/

micromechanical formulation that accounts for the formation of air voids and progressive damage was derived. The present micromechanics-based model was implemented into a finite element (FE) code to estimate the damage parameters of the composites. Based on the proposed model, a series of numerical simulations were carried out to assess the influence of damage parameters and air voids on the overall behavior of the composites. Finally, the FRP composites were attached to the bottom of a reinforced concrete (RC) beam, and a four-point loading test was then carried out. The results obtained by means of micromechanical modeling and FE implementation were compared to experimental data obtained from RC beams strengthened with the random-chopped FRP composites.

2. Material properties of random-chopped FRP composites

2.1. Materials and specimens

The composite used in this study consists of 2D randomly oriented chopped E-glass fibers in an epoxy resin matrix [19]. The elastic properties of E-glass fibers and epoxy resin are $E_0 = 1.3$ GPa, $\upsilon_0 = 0.3$; $E_1 = 72.5$ GPa, $\upsilon_1 = 0.2$, where E_q and υ_q ($q = 0, 1$) denote the Young's modulus and the Poisson's ratio of the epoxy matrix and chopped fibers, as listed in Table 1.

The random-chopped FRP composite was fabricated by following the multi-spray lay-up process and more details about this process can be found in [20]. Key variables are the bundle fiber lengths (30 and 60 mm) and the volume fractions of the fibers (10% and 25% in volume). The specimens are classified as follow: C-30L-10V, C-30L-25V, and C-60L-25V, where 'C', 'L' and 'V' denote the coupon-shaped specimen, length of the fiber and the volume fraction of fibers, respectively. The fabricated composites were cured for 2 weeks under atmospheric pressure condition and a normal ambient curing temperature of 23 °C. The manufactured composites were then cut into coupon shaped specimens with geometry Type 3 in accordance with ASTM D638 [21].

2.2. Testing procedures and results

To evaluate the mechanical properties of the random-chopped FRP composite containing air voids, a series of tensile tests were carried out in accordance with ASTM D 638 [21]. The tensile strength tests were conducted using 100 kN capacity load cell connected to INSTRON 4482 machine to measure the applied loads and strain values. Details of test methodology and relevant apparatus can be found in ASTM D 638 [21]. In addition, the results of tensile experiments on the composites are given in Table 2.

The air voids in composites was also experimentally measured by a microscope image program (MicroCapture Software) as shown in Fig. 1(a). Before measuring the air voids, polishing was progressively conducted with No. 400, 600, 1000, and 1200 abrasive sandpaper on a composite surface to ensure a consistent quality of the surface condition, as recommended by [22]. Three microscope images of each specimen were taken at a side surface within the gauge length in the longitudinal direction using a microscope camera (UC-CAM 220B). From microscope images taken under magnification of ×195, three different phases composed of the matrix, voids, and chopped glass fibers were observed. The void phase has an approximately spherical shape with various diameters, while the chopped glass fibers have various elliptical shapes in the matrix, as shown in Fig. 1(a). To measure the void contents in the composites specimens, the statistical void percentage in the microscope images was taken as equal to the volume percentage of the voids [11,23]. With respect to the C-30L-10V, C-30L-25V, and C-60L-25V specimens, the volume fraction of the void phase was measured as: 10.09%, 10.36%, and 10.73%, respectively, as shown in Fig. 1 and Table 3.

Table 1
The elastic properties of E-glass fiber and epoxy resin.

Material	Modulus of elasticity (GPa)	Poisson's ratio
E-glass	7.25	0.2
Epoxy resin	1.30	0.3

Table 2
Measured ultimate stress and strain of coupon specimens.

Specimen	Strain (%)	Ultimate stress (MPa)
C-30L-10P Average	4.11	28.50
C-30L-25P Average	4.75	33.07
C-60L-25P Average	2.99	36.36

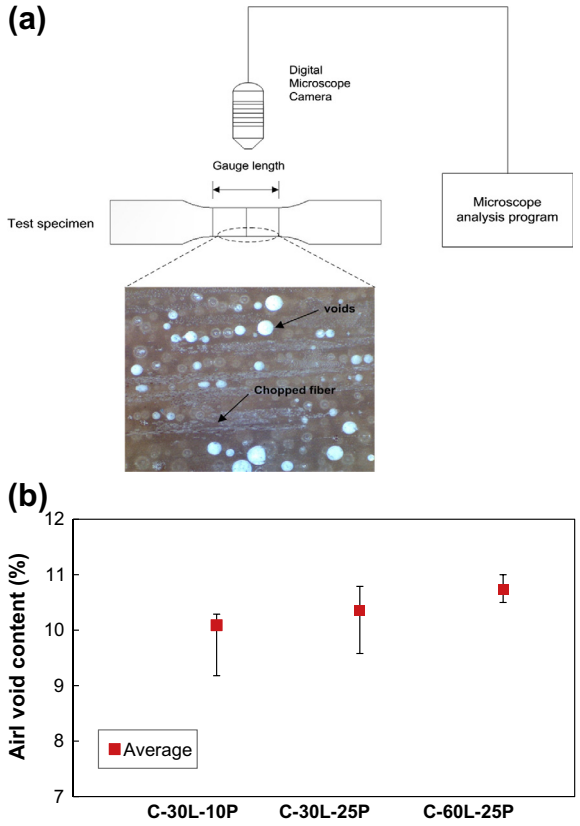

Fig. 1. (a) Scheme of the microscope image analysis (the cross-section of air voids and chopped fibers) and (b) the measured void contents of each specimen.

Table 3
Statistical results of measured volume fraction of voids for each specimen.

Specimen	Average (%)	Standard deviation	Coefficient of variation (%)
C-30L-10P	10.09	0.88	8.74
C-30L-25P	10.36	0.52	5.01
C-60L-25P	10.73	0.25	2.34

3. Modeling of random-chopped fiber-reinforced polymer composites

3.1. Micromechanical constitutive equation considering voids

Random-chopped FRP composites are assumed to be comprised of a polymer matrix (phase 0), discontinuous fibers with different levels of damage (phases 1, 2, 3, and 4). In addition, for a more realistic estimation of the random-chopped FRP composites, spherical voids (phase 5), which are uniformly dispersed in the matrix, are additionally considered in the present study. The effective stiffness tensor $\mathbf{C}^*$ of the composites containing unidirectionally aligned fibers can then be derived as follows [24,25]:

$$\mathbf{C}^* = \mathbf{C}_0 \cdot \left[\mathbf{I} + \sum_{q=1}^{5}\left\{\phi_q(\mathbf{A}_q + \mathbf{S}_q)\cdot\left[\mathbf{I} - \phi_q\mathbf{S}_q\cdot(\mathbf{A}_q+\mathbf{S}_q)^{-1}\right]^{-1}\right\}\right] \tag{1}$$

with

$$\mathbf{A}_q = (\mathbf{C}_q + \mathbf{C}_0)\cdot\mathbf{C}_0 \tag{2}$$

Here, $\mathbf{I}$ is the fourth-rank identity tensor, $\mathbf{C}_q$ and ϕ_q are the elasticity tensor and volume fraction of the q-phase, respectively [26,27]. $\mathbf{S}_q$ is the Eshelby's tensor of the q-phase [28], and the components of second-rank Eshelby's tensors $\mathbf{S}_{1,\cdots,5}$ can be found in [29]. With the help of the Eshelby's tensor, the effective elasticity tensor $\mathbf{C}^*$ for the six-phase composites containing unidirectionally aligned fibers can be written as

$$\mathbf{C}^* = C_{IK}^{(1)}\delta_{ij}\delta_{kl} + C_{IJ}^{(2)}(\delta_{ik}\delta_{jl} + \delta_{il}\delta_{jk}) \tag{3}$$

in which

$$C_{IK}^{(1)} = 2\lambda_0\chi_{KK}^{(2)} + 2\mu_0\chi_{IK}^{(1)} + \lambda_0\sum_{n=1}^{3}\chi_{nK}^{(1)}, \quad C_{IJ}^{(2)} = 2\mu_0\chi_{IJ}^{(2)} \tag{4}$$

where λ_0, μ_0 are the Láme constants of the matrix, and the components $\chi_{IK}^{(1)}$ and $\chi_{IJ}^{(2)}$ are given in Appendix A. In order to obtain an effective constitutive equation of the random-chopped FRP composites, an effective elasticity tensor $\mathbf{C}^*$ containing unidirectionally aligned fibers in Eq. (3) should be applied to the average process over all orientations in the 1–2 plane as [30,31]

$$\langle\mathbf{M}\rangle = \frac{1}{\pi}\int_0^{\pi} c_{ip}c_{iq}c_{kr}c_{ls}M_{ijkl}\,\mathrm{d}\theta \tag{5}$$

In this equation, $\langle\cdot\rangle$ signifies the 2D orientational average process and c_{ip} denotes the direction cosines [31]. According to the orientational average procedure, the overall stiffness tensor of the random-chopped FRP composites assumed as 2D randomly oriented discontinuous fiber-reinforced composites with spherical voids can be obtained as

$$\mathbf{C}^* = \widehat{C}_{IK}^{(1)}\delta_{ij}\delta_{kl} + \widehat{C}_{IJ}^{(2)}(\delta_{ik}\delta_{jl} + \delta_{il}\delta_{jk}) \tag{6}$$

where the second-rank tensors $\widehat{C}_{IK}^{(1)}$ and $\widehat{C}_{IJ}^{(2)}$ are given in Appendix B.

Furthermore, the damage mechanism proposed by [32] is adopted in the present study. The multi-level damage model is expressed as the current volume fraction of fibers in the q-phase in the following probability function, as in several earlier studies [29,33]:

$$\phi_3 = \bar{\phi}_3 - \phi_4, \quad \phi_2 = \bar{\phi}_2 - \bar{\phi}_3, \quad \phi_1 = \phi - \bar{\phi}_2 \tag{7}$$

with

$$\bar{\phi}_2 = \phi\left[1 - \exp\left\{-\left(\frac{\bar{\sigma}_f}{S_0}\right)^M\right\}\right], \bar{\phi}_3 = \bar{\phi}_2\left[1 - \exp\left\{-\left(\frac{\bar{\sigma}_f}{S_0}\right)^M\right\}\right],$$
$$\bar{\phi}_4 = \bar{\phi}_3\left[1 - \exp\left\{-\left(\frac{\bar{\sigma}_f}{S_0}\right)^M\right\}\right] \tag{8}$$

Here, ϕ and $\bar{\sigma}_f$ are the original volume fraction and the averaged internal stress of the fiber; S_0 and M are the model parameters. Based on the averaged internal stress of the aligned fiber $\bar{\sigma}_f$ proposed by [34], we adopt a 2D randomly oriented averaged internal stress of reinforcements $\langle\bar{\sigma}_f\rangle$, as follows [34]:

$$\langle\bar{\sigma}_f\rangle = \left[\mathbf{C}_1\cdot\left\{\mathbf{I} - \mathbf{S}_1\cdot(\mathbf{A}_1+\mathbf{S}_1)^{-1}\right\}\cdot\left\{\mathbf{I} - \sum_{q=1}^{5}\phi_q\mathbf{S}_q(\mathbf{A}_q+\mathbf{S}_q)^{-1}\right\}^{-1}\right] :$$
$$\bar{\varepsilon} \equiv \left[\widehat{U}_{IK}^{(1)}\delta_{ij}\delta_{kl} + \widehat{U}_{IJ}^{(2)}(\delta_{ik}\delta_{jl} + \delta_{il}\delta_{jk})\right] : \bar{\varepsilon} \tag{9}$$

where the second-rank tensors $\widehat{U}_{IK}^{(1)}$ and $\widehat{U}_{IJ}^{(2)}$ are given in Appendix C.

3.2. FE analysis for evaluating the damage parameters

A FE model of coupon-shaped specimen was created (Fig. 2.) to determine the model parameters of damage (S_0 and M) by comparing predicted uniaxial tensile responses and experimental results (CL-30L-10V, CL-30L-25V, CL-60L-25V). The proposed micromechanical model was implemented into the FE code ABAQUS Standard Version 6.5 via its user subroutine UMAT [35,36]. The following constituent properties were adopted: $E_0 = 1.3$ GPa, $\upsilon_0 = 0.3$; $E_1 = 72.5$ GPa, $\upsilon_1 = 0.2$, where E_q and υ_q ($q = 0, 1$) denote the Young's modulus and the Poisson's ratio of the epoxy matrix and chopped fibers. The volume fractions of the air void were determined in accordance with the experimentally obtained values (cf. Fig. 1).

The aspect ratio of discontinuous fibers (γ) is determined as follows:

$$\gamma = \frac{l_f}{d_{bundle}} \tag{10}$$

where d_{bundle} is the effective diameter of bundle fibers, and is calculated in accordance with the simple model proposed by [37], denoted as

$$d_{bundle} = \sqrt{N(d_{filament})^2/\phi_{filament}} \tag{11}$$

where N is number filament of glass fibers, $d_{filament}$ is diameter of the single filament that is measured as 11 μm, and $\phi_{filament}$ is the volume fraction of filaments within a fiber bundle which is assumed to be 0.6, as recommended by [37]. The effective diameter and

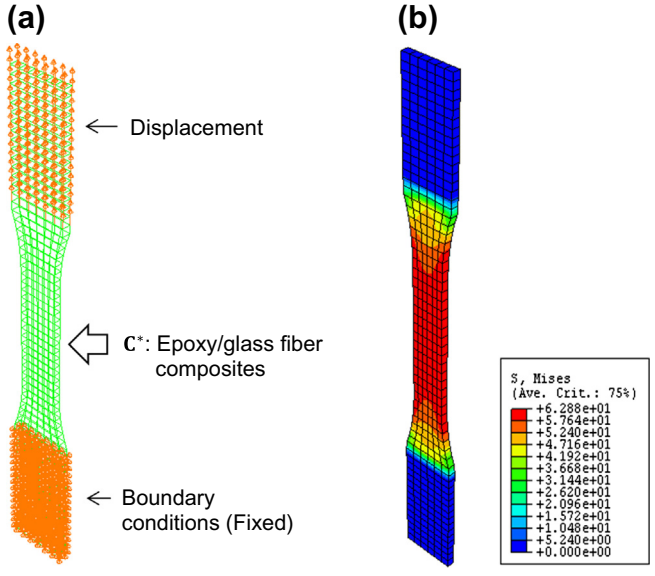

Fig. 2. (a) The FE model of coupon-shaped specimen and (b) the representative von-Mises stress distribution of the random-chopped FRP composites.

aspect ratio $\gamma = (l/d_{bundle})$ of the glass fibers with respect to fiber length are summarized in Table 4.

A series of numerical test results are briefly presented to elucidate the proposed formulation. The focus of the numerical test is on uniaxial tension in the longitudinal direction with different model constants, such as damage parameters (S_0 and M) and air voids (ϕ_5). First, a parametric analysis of the S_0 and M were examined, as shown in Fig. 3(a). The stress–strain response of the discontinuous fiber-reinforced composites becomes stiffer as the damage parameter S_0 increases, while a lower effective stiffness of the composites was observed as the M value increases. It denotes that the interfacial damage gradually occurs earlier as S_0 decreases and M increases [38,39]. Furthermore, to examine the effect of air voids on the composites, the predicted Young's modulus and the corresponding stress–strain curves with different contents of air voids are illustrated in Fig. 3(b). Increase in the volume fraction of air voids weakens the stiffness of the composites and therefore lowers the stress–strain behavior of the composites [40]. Furthermore, the effects of aspect ratio and volume fraction of fibers are illustrated in Fig. 4. It is shown in Figs. 4(a) and (b) that higher aspect ratio γ and volume fraction of short fibers ϕ lead to a stiffer stress–strain response. In addition, the predicted damage evolution curves of the composites corresponding to Fig. 4 are provided in Fig. 5. It is seen from Fig. 5(a) and (b) that the aspect ratio and the volume fraction of fibers have a considerable influence on the damage evolution, and the chopped fibers evolve more rapidly to damage fibers as the aspect ratio increases and the volume fraction of fibers decreases.

The damage parameters are initially estimated to be S_0 = 250 MPa and M = 0.5 via a curve fitting with the experimentally measured stress–strain response of coupon-shaped specimens (CL-30L-10V). The same values as the established damage parameters (S_0 = 250 MPa and M = 0.5) are then applied to CL-30L-25V

Table 4
The effective diameter of bundle fiber and bundle fiber aspect ratio.

Fiber length (mm)	Number filament of glass fibers, N	The diameter of bundle fiber (mm), d_{bundle}	Bundle fiber aspect ratio, γ
30	119	0.155	194
60	119	0.155	387

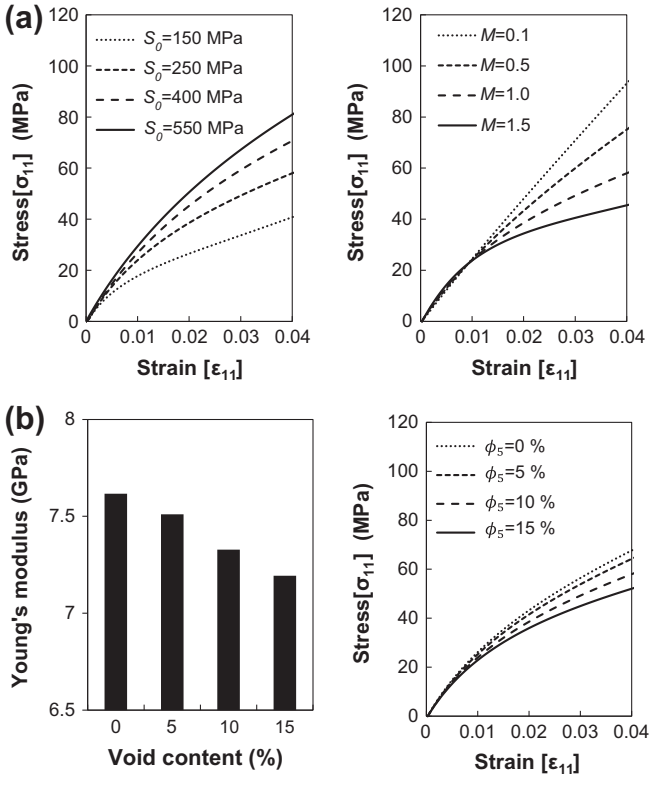

Fig. 3. The numerical simulation results (S_0 = 150 MPa, M = 0.5, l_f = 60 mm, ϕ = 10 %, ϕ_5 = 10%): (a) the predicted stress–strain responses of composites with varying damage parameters and (b) the predicted Young's modulus of composites with respect to void contents and the corresponding stress–strain curves.

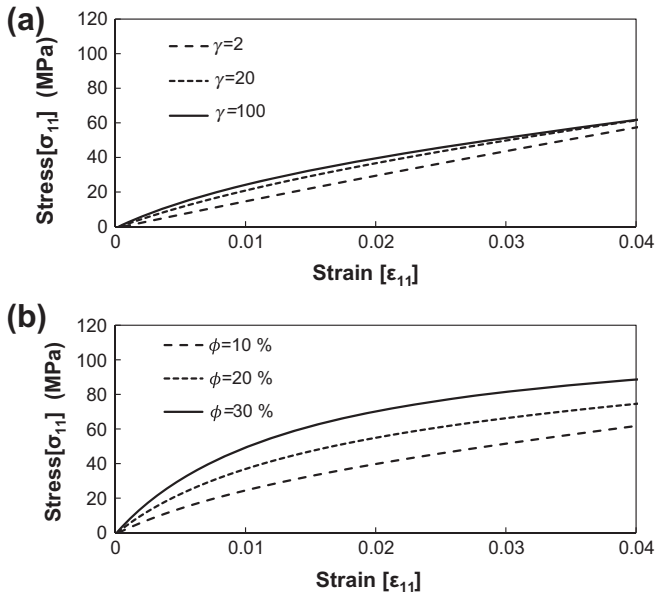

Fig. 4. The predicted stress–strain curves of composites with various aspect ratio values (a), volume fraction of the fiber reinforcements (b).

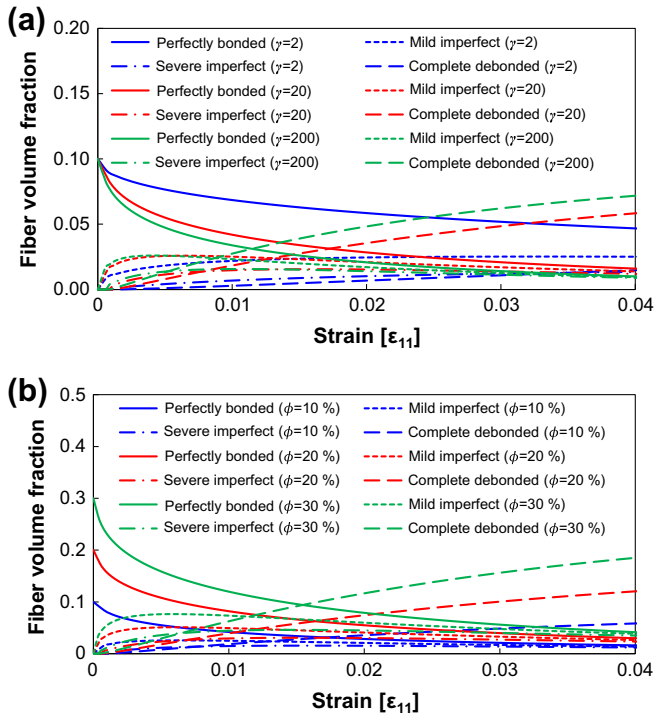

Fig. 5. The predicted damage evolution curves of the composites corresponding to Fig. 4.

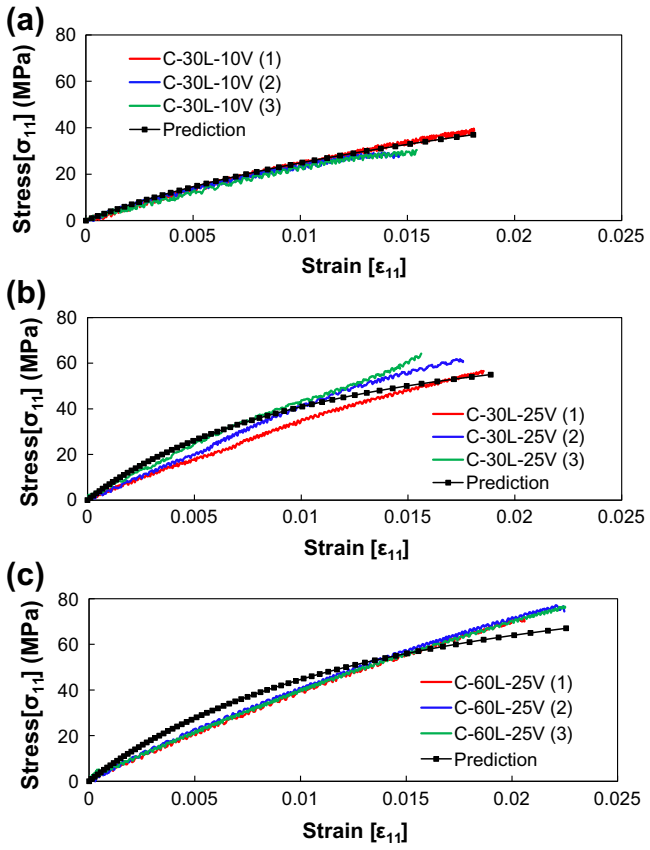

Fig. 6. Comparisons between the present predictions (S_0 = 250 MPa, M = 0.5) and experimental data (a) C-30L-10V, (b) C-30L-25V and (c) C-60L-25V for the overall uniaxial tensile responses of the random-chopped FRP composites.

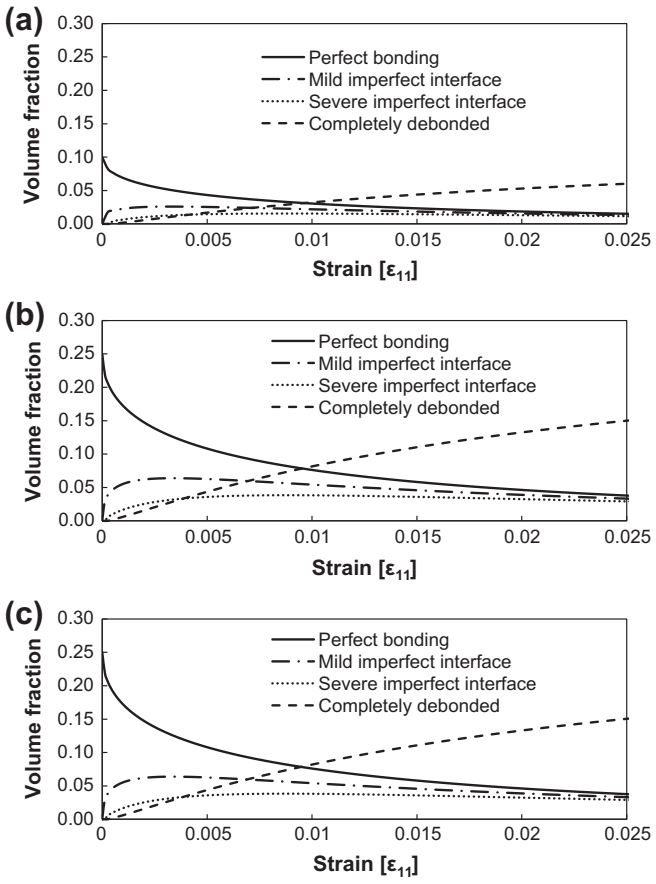

Fig. 7. The predicted evolution of perfectly bonded fibers, fibers with a mildly imperfect interface, fibers with a severely imperfect interface, and completely debonded fibers corresponding to Fig. 5 for C-30L-10V (a), C-30L-25V (b), and C-60L-25V (c).

and CL-60L-25V cases. Fig. 6(a–c) shows the comparisons between the predicted stress–strain curves of the random-chopped FRP composites under uniaxial tension and the experimental results of coupon shaped specimens with different lengths and volume fractions of fibers (C-30L-10V, C-30L-25V, and C-60L-25V). It can be observed in Fig. 6 that the predicted mechanical behaviors of the composites were in good agreement with the experimental data. It should be noted that the same values of damage parameters were applied to all cases regardless of the constituent properties for the comparison, and this was also done to verify the present framework and to ensure the predictive capability of the proposed model. The predicted progression of volume fractions of perfectly bonded fibers and different level of damaged fibers corresponding to Fig. 6 is shown in Fig. 7.

4. Experiments and FE analysis on strengthening performance of random-chopped FRP composites

The strengthening performance is also predicted by implementing the proposed model into a finite element (FE) code. A comparative study between the present experimental data and the predicted results is conducted to assess the predictive capability of the analysis tool using the proposed micromechanics-based damage model for RC beams strengthened with the random-chopped FRP composite.

4.1. Strengthening performance: Experiments

A series of static four-point bending tests were conducted on rectangular specimens to investigate the strengthening performance of reinforced concrete specimens strengthened with the random-chopped FRP composite. A total of 9 RC beams with cross-sections of 100 mm × 100 mm were produced over an effective span of 457 mm [41]. The random-chopped FRP composite consisting of various constituents (S-30L-10V, S-30L-25V, and S-60L-25V) was applied on RC specimens up to target thicknesses of 4 mm by the multi-spray lay-up process. Here, 'S', 'L', and 'V' denote the strengthened RC beam, the length of the fiber, and the volume fraction of fibers, respectively. The test results of the experimental data are summarized in Table 5.

4.2. FE modeling and experimental comparisons

The strengthening performance of the specimens (S-30L-10V, S-30L-25V, S-60L-25V) was predicted by implementing the

Table 5
Measured deflection and ultimate load of strengthened RC beams.

Specimen	δ_{ult} (mm)	P_{ult} (kN)
S-30L-10V	4.73	31.53
	3.53	26.00
	4.07	27.97
Average	4.11	28.50
S-30L-25V	5.95	37.94
	5.32	29.53
	2.98	31.73
Average	4.75	33.07
S-60L-25V	3.40	40.10
	3.17	36.96
	2.40	32.02
Average	2.99	36.36

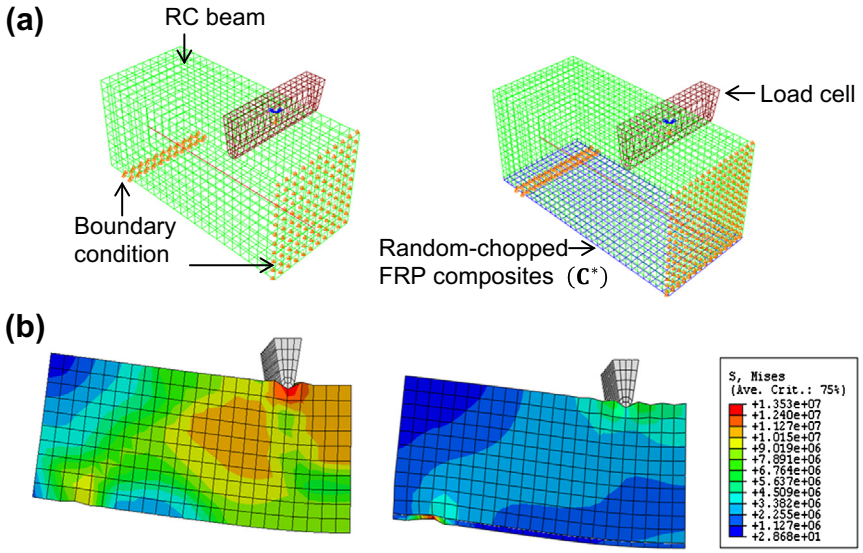

Fig. 8. (a) FE meshes of a control beam and a strengthen beam with random-chopped FRP composites (S-30L-10V, S-30L-25V, and S-60L-25 V) and (b) the representative deformed shape and von-Mises effective stress of a control beam and a RC beam strengthen with composites during four-point bending tests.

developed model into the FE code ABAQUS. Since the fundamental behavior of concrete material cannot be stimulated through the present micromechanical model, the smeared crack approach [35] was used to analyze the plain concrete. The material properties of concrete were sourced from [37], and the concrete model parameters were fitted to the experimentally measured load–displacement curves of the plain concrete (control beam). The Young's modulus and the Poisson's ratio of the steel rebar are 200 GPa and 0.3, respectively.

Fig. 8(a) illustrates a FE mesh of the specimens, RC beam consisting of 3D solid elements (C3D8R) and truss bar elements (T3D2) was formulated as the control beam. In addition, the strengthened RC beam with the random-chopped FRP was modeled, where the overlaid 3D solid elements on the bottom of the control beam represents the random-chopped FRP. For a less expensive calculation, the FE meshes in the analysis were modeled as a half of the specimen. The representative deformed shape and von-Misses effective stress of control and RC beam strengthened by the composites during the four-point loading are displayed in Fig. 8(b).

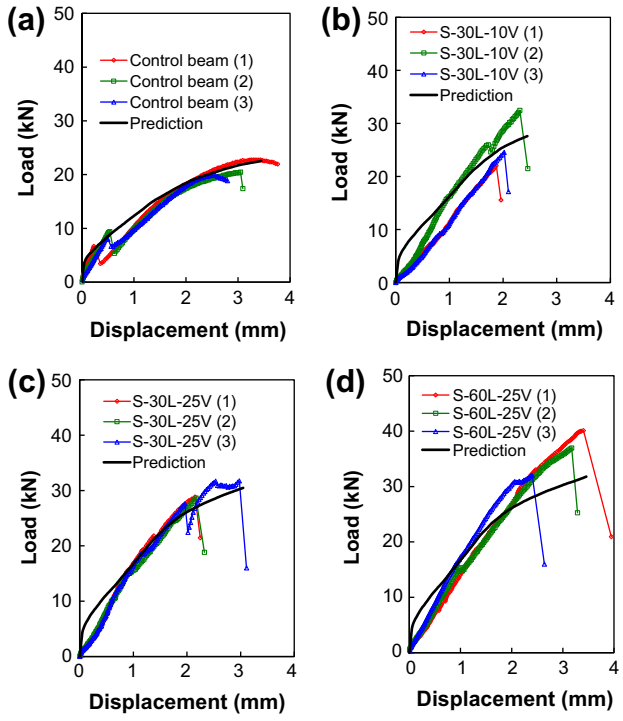

Fig. 9. The comparisons of load–displacement curves between the present prediction and the experimental data of (a) control beam, (b) S-30L-10V, (c) S-30L-25V and (d) S-60L-25 V.

The comparisons between the predictions based on the proposed model and the RC beam strengthened with the random-chopped FRP consisting various lengths and volume fractions of fibers are presented in Fig. 9. In particular, the load–displacement curves of control beams in Fig. 9(a) show a discontinuous behavior since cracks on a soffit of the specimens occurred at an early loading stage. In addition, the load–displacement curves of the S-30L-10V (2) and S-30L-25V (3) specimens exhibit an abrupt drop near a displacement of 2 mm, which is caused by an initial cracking of concrete beams [42]. With an increasing load, S-30L-10V (2) specimen finally failed due to a rupture of the random-chopped FRP composite, while S-30L-25V (3) specimen reached to rupture failure along with interfacial debonding of the composite in the post-cracking range [42,43].

It should be noted that the same damage parameters previously used (S_0 = 250 MPa, M = 0.5) were utilized again in this comparison to verify the model. It is clearly shown in Fig. 9 that the random-chopped FRP confinement serves to improve the load carrying capacity of the RC beam. Moreover, the instances of good agreement between the present predictions and various results from the experimental data show the predictive capability of the proposed framework for the random-chopped FRP composites.

5. Concluding remarks

The experimental and theoretical investigations on the random-chopped FRP composites containing high volume fraction of air voids have been presented in this paper. A series of tensile and four-point bending tests were carried out in accordance with related standards, and the experimental results were used for comparisons with the predictions according to the micromechanics and FE methodology for the composites. The following conclusions can be drawn concerning the present study:

(1) The air void affects the overall behavior of the random-chopped FRP composites, indicating that a higher volume fraction of voids leads to a lower effective stiffness of the composites.
(2) The volume fraction of voids in the FRP composites manufactured by the spray lay-up process was generally measured as 10–11%.
(3) The aspect ratio and volume fraction of the fibers has a significantly effect on the composites: the large aspect ratio and the high volume fraction of the chopped fibers result in stiffer composite materials, giving a higher stress/strain ratio.
(4) The damage parameters in the proposed model are estimated by comparing predicted uniaxial tensile responses and experimental results as $S_0 = 250$ MPa and $M = 0.5$.
(5) RC beams retrofitted with the random-chopped FRP composites have higher load carrying capacity than neat RC beams, verifying that the composite coating can be used as a strengthening method for existing structures.

The proposed framework is versatile and could be applied to various composite materials. In the future, the predictions will be further compared with additional experiments under different loading tests and boundary conditions. Additional physical characteristics such as thermal properties [44], crack evolutions [45], and viscoelastic behaviors [46] should be taken into account for more realistically predictions of the thermal stability and the strain-rate dependent behavior of the composites.

Acknowledgements

This research was supported by a Grant (13SCIPA01) from Smart Civil Infrastructure Research Program funded by Ministry of Land, Infrastructure and Transport (MOLIT) of Korea government and Korea Agency for Infrastructure Technology Advancement (KAIA).

Appendix A

Parameters $\chi_{IK}^{(1)}$ and $\chi_{IJ}^{(2)}$ in Eq. (4)

$$\begin{aligned}\chi_{IK}^{(1)} &= \psi_{IK}^{(1)} + \psi_{IK}^{(3)} + \psi_{IK}^{(5)} + \psi_{IK}^{(7)} + \psi^{(9)},\\ \chi_{IJ}^{(2)} &= \frac{1}{2}\psi_{IJ}^{(2)} + \psi_{IJ}^{(4)} + \psi_{IJ}^{(6)} + \psi_{IJ}^{(8)} + \psi^{(10)}\end{aligned} \tag{A.1}$$

where the components $\psi_{IK}^{(2q-1)}$ and $\psi_{IJ}^{(2q)}$ are given in [27], and the parameters $\psi^{(9)}$ and $\psi^{(10)}$ can be expressed as

$$\psi^{(9)} = \phi_5\left[2\eta^{(10)} + \omega^{(9)} + \eta^{(9)}\{3\omega^{(9)} + 2\omega^{(10)}\}\right], \quad \psi^{(9)} = 2\phi_5\eta^{(10)}\omega^{(10)} \tag{A.2}$$

with

$$\omega^{(9)} = \frac{\xi^{(9)}}{(2\xi^{(10)} - 1)(3\xi^{(9)} + 2\xi^{(10)} - 1)}, \quad \omega^{(10)} = \frac{1}{2 - 4\xi^{(10)}} \tag{A.3}$$

in which

$$\xi^{(9)} = -\left[\frac{5\eta^{(9)}(1+\nu_0) + 2\eta^{(10)}(5\nu_0 - 1)\phi_5}{15(\nu_0 - 1)}\right], \quad \xi^{(10)} = \frac{2\eta^{(10)}(5\nu_0 - 1)\phi_5}{15(\nu_0 - 1)} \tag{A.4}$$

in which

$$\eta^{(9)} = \frac{1}{4}\left[3 + \frac{1}{2\nu_0 - 1} + \frac{8}{5\nu_0 - 7}\right], \quad \eta^{(10)} = \frac{3}{7 - 5\nu_0} - \frac{3}{2} \tag{A.5}$$

where ν_0 is the Poisson's ratio of the matrix.

Appendix B

Parameters $\widehat{C}_{IK}^{(1)}$ and $\widehat{C}_{IJ}^{(1)}$ in Eq. (6)

$$\begin{aligned}&\widehat{C}_{11}^{(1)} = \widehat{C}_{12}^{(1)} = \widehat{C}_{21}^{(1)} = \widehat{C}_{22}^{(1)} = \tfrac{1}{8}\begin{bmatrix} C_{11}^{(1)} + 3C_{12}^{(1)} + 3C_{21}^{(1)} + C_{22}^{(1)} \\ +2C_{11}^{(2)} - 4C_{12}^{(2)} + 2C_{22}^{(2)}\end{bmatrix}\\ &\widehat{C}_{13}^{(1)} = \widehat{C}_{23}^{(1)} = \tfrac{1}{2}\left[C_{12}^{(1)} + C_{22}^{(1)}\right], \widehat{C}_{31}^{(1)} = \widehat{C}_{32}^{(1)} = \tfrac{1}{2}\left[C_{21}^{(1)} + C_{22}^{(1)}\right], \widehat{C}_{33}^{(1)} = C_{33}^{(1)}\\ &\widehat{C}_{11}^{(2)} = \widehat{C}_{12}^{(2)} = \widehat{C}_{21}^{(2)} = \widehat{C}_{22}^{(2)} = \tfrac{1}{8}\begin{bmatrix} C_{11}^{(1)} - C_{12}^{(1)} - C_{21}^{(1)} + C_{22}^{(1)} \\ +2C_{11}^{(2)} + 4C_{12}^{(2)} + 2C_{22}^{(2)}\end{bmatrix}\\ &\widehat{C}_{13}^{(2)} = \widehat{C}_{31}^{(2)} = \widehat{C}_{23}^{(2)} = \widehat{C}_{32}^{(2)} = \tfrac{1}{2}[C_{12}^{(2)} + C_{22}^{(2)}], \widehat{C}_{33}^{(2)} = C_{33}^{(2)}\end{aligned} \tag{B.1}$$

where the components $C_{IK}^{(1)}$ and $C_{IJ}^{(2)}$ are given in Eq. (4).

Appendix C

Parameters $\widehat{U}_{IK}^{(1)}$ and $\widehat{U}_{IJ}^{(1)}$ in Eq. (9)

$$\begin{aligned}&\widehat{U}_{11}^{(1)} = \widehat{U}_{12}^{(1)} = \widehat{U}_{21}^{(1)} = \widehat{U}_{22}^{(1)} = \tfrac{1}{8}\begin{bmatrix} U_{11}^{(1)} + 3U_{12}^{(1)} + 3U_{21}^{(1)} + U_{22}^{(1)} \\ +2U_{11}^{(2)} - 4U_{12}^{(2)} + 2U_{22}^{(2)}\end{bmatrix}\\ &\widehat{U}_{13}^{(1)} = \widehat{U}_{23}^{(1)} = \tfrac{1}{2}\left[U_{12}^{(1)} + U_{22}^{(1)}\right], \widehat{U}_{31}^{(1)} = \widehat{U}_{32}^{(1)} = \tfrac{1}{2}\left[U_{21}^{(1)} + U_{22}^{(1)}\right], \widehat{U}_{33}^{(1)} = U_{33}^{(1)}\\ &\widehat{U}_{11}^{(2)} = \widehat{U}_{12}^{(2)} = \widehat{U}_{21}^{(2)} = \widehat{U}_{22}^{(2)} = \tfrac{1}{8}\begin{bmatrix} U_{11}^{(1)} - U_{12}^{(1)} - U_{21}^{(1)} + U_{22}^{(1)} \\ +2U_{11}^{(2)} + 4U_{12}^{(2)} + 2U_{22}^{(2)}\end{bmatrix}\\ &\widehat{U}_{13}^{(2)} = \widehat{U}_{31}^{(2)} = \widehat{U}_{23}^{(2)} = \widehat{U}_{32}^{(2)} = \tfrac{1}{2}[U_{12}^{(2)} + U_{22}^{(2)}], \widehat{U}_{33}^{(2)} = U_{33}^{(2)}\end{aligned} \tag{C.1}$$

where the second-rank tensors $U_{IK}^{(1)}$ and $U_{IJ}^{(2)}$ are listed in [29].

References

[1] Wang Y, Yang LJ, Wang NJ. An investigation of laser-assisted machining of Al_2O_3 particle reinforced aluminum matrix composite. J Mater Process Technol 2002;129(1–3):268–72.
[2] Lee HK, Pyo SH. Micromechanics-based elastic damage modeling of particulate composites with weakened interfaces. Int J Solids Struct 2007;44(25–26):8390–460.
[3] Lee HK, Ju JW. A three-dimensional stress analysis of penny-shaped crack interacting with a spherical inclusion. Int J Damage Mech 2007;16(3):331–59.
[4] Yang BJ, Shin H, Lee HK, Kim H. A combined molecular dynamics/micromechanics/finite element approach for multiscale constitutive modeling of nanocomposites with interface effects. Appl Phys Lett 2013;103:241903.
[5] Kim BR, Ha SK, Na S, Lee HK. Application of FRP composites for rehabilitation in civil engineering: experiments and advanced computational methods. Nova Science Publishers; 2012.
[6] Lee HK, Simunovic S. Modeling of progressive damage in aligned and randomly oriented discontinuous fiber polymer matrix composites. Compos Part B-Eng 2000;31(2):77–86.
[7] Lee HK, Simunovic S. A damage constitutive model of progressive debonding in aligned discontinuous fiber composites. Int J Solids Struct 2001;38(5):875–95.
[8] Lee HK, Pyo SH. An elastoplastic multi-level damage model for ductile matrix composites considering evolutionary weakened interface. Int J Solids Struct 2008;45(6):1614–31.
[9] Rousakis TC, Karabinis AI, Kiousis PD. FRP-confined concrete members: axial compression experiments and plasticity modeling. Eng Struct 2007;29(7):1343–53.
[10] Bakis CE, Bank LC, Brown VL, Cosenza E, Davalos JF, Lesko JJ. Fiber-reinforced polymer composites for construction—state-of-the-art review. ASCE J Compos Constr 2002;6(2):73–87.
[11] Suhot MA, Chambers AR. The effect of voids on the flexural fatigue performance of unidirectional carbon fibre composites. The 16th International Conference on Composite Materials, Kyoto, Japan; 2007.
[12] Lee HK, Hausmann LR. Structural repair and strengthening of damaged RC beams with sprayed FRP. Compos Struct 2004;63(2):201–9.
[13] Danas K, Aravas N. Numerical modeling of elasto-plastic porous materials with void shape effects at finite deformations. Compos Part B-Eng 2012;43(6):2544–59.
[14] Boyd AJ, Liang N, Gree P, Lammert K. Sprayed FRP repair of simulated impact in prestressed concrete girders. Constr Build Mater 2008;22(3):411–6.
[15] Agius SL, Magniez KJC, Fox BL. Cure behaviour and void development within rapidly cured out-of-autoclave composites. Compos Part B-Eng 2013;47:230–7.
[16] Liu L, Zhang B, Wu Z, Wang D. Effects of cure pressure induced voids on the mechanical strength of carbon/epoxy laminates. J Mater Sci Technol 2005;21(1):87–91.

[17] Hollaway LC. Handbook of polymer composites for engineers. The British Plastics Federation; 1994.
[18] Karabutov AA, Podymova NB. Quantitative analysis of the influence of voids and delaminations on acoustic attenuation in CFRP composites by the laser-ultrasonic spectroscopy method. Compos Part B-Eng 2013;47:230–7.
[19] Ha SK, Na S, Bang YK, Lee HK. An experimental study on sag-resistance ability and applicability of sprayed FRP system on vertical and overhead concrete surfaces. Mater Struct 2013. http://dx.doi.org/10.1617/s11527-013-0165-7.
[20] Ha SK, Na S, Lee HK. Bond characteristics of sprayed FRP composites bonded to concrete substrate considering various concrete surface conditions. Compos Struct 2013;100:270–9.
[21] ASTM D 638. Standard test method for tensile properties of plastics; 2010.
[22] Zhu H, Wu B, Li D, Zhang D, Chen Y. Influence of voids on the tensile performance of carbon/epoxy fabric laminates. J Mater Sci Technol 2011;27(1):69–73.
[23] Ghiorse SR. Effect of void content on the mechanical properties of carbon/epoxy laminates. SAMPE Quartely 1993;24:54–9.
[24] Ju JW, Chen TM. Micromechanics and effective elastoplastic behavior of two-phase metal matrix composites. J Eng Mater-T ASME 1994;116(3):310–8.
[25] Yang BJ, Kim BR, Lee HK. Micromechanics-based viscoelastic damage model for particle-reinforced polymeric composites. Acta Mech 2012;223(6):1307–21.
[26] Kim BR, Lee HK. Elastic-damage modeling for particulate composites considering cumulative damage. Int J Damage Mech 2011;20(1):131–58.
[27] Yang BJ, Kim BR, Lee HK. Predictions of viscoelastic strain-rate dependent behavior of fiber-reinforced polymeric composites. Compos Struct 2012;94(4):1420–9.
[28] Eshelby JD. The determination of the elastic field of an ellipsoidal inclusion, and related problems. P Roy Soc A-Math Phy 1957;241(1226):376–96.
[29] Pyo SH, Lee HK. Micromechanical analysis of aligned and randomly oriented whisker-/short fiber-reinforced composites. CMES-Comp Model Eng 2009;40(3):271–305.
[30] Marzari N, Ferrari M. Textural and micromorphological effects on the overall elastic response of macroscopically anisotropic composites. J Appl Mech-T ASME 1992;59(2):269–75.
[31] Lee HK, Simunovic S. Prediction of crack evolution and effective elastic behavior of damage-tolerant brittle composites. Comput Method Appl M 2006;196(1–3):118–33.
[32] Lee HK, Pyo SH. Multi-level modeling of effective elastic behavior and progressive weakened interface in particulate composites. Compos Sci Technol 2008;68(2):387–97.
[33] Weibull W. A statistical distribution function of wide applicability. J Appl Mech-T ASME 1951;18:293–7.
[34] Ju JW, Lee HK. A micromechanical damage model for effective elastoplastic behavior of ductile matrix composites considering evolutionary complete particle debonding. Comput Method Appl M 2000;183(3–4):201–22.
[35] ABAQUS Version 6.5. Hibbitt, Karlsson & Sorensen: RisingSun Mills; 2005.
[36] Liang Z, Lee HK, Suaris W. Micromechanics-based constitutive modeling for unidirectional laminated composites. Int J Solids Struct 2006;43(18–19):5674–89.
[37] Ha SK. Advanced spray-up retrofitting of concrete: improved lay-up process and tensile/bond characteristics of spray-up FRP in concrete. Ph D. thesis, Korea Advanced Institute of Science and Technology (KAIST); 2012.
[38] Pyo SH, Lee HK. Micromechanics-based elastic-damage analysis of laminated composite structures. Int J Solids Struct 2009;46(17):3138–49.
[39] Yang BJ, Hwang YY, Lee HK. Elastoplastic modeling of polymeric composites containing randomly located nanoparticles with an interface effect. Compos Struct 2013;99:123–30.
[40] Lee HK, Kim BR, Ha SK. Numerical evaluation of shear strengthening performance of FRP sheets/strips and sprayed FRP coating repair systems. Compos Part B-Eng 2008;39(5):851–62.
[41] Tawie R, Lee HK, Park SH. Non-destructive evaluation of concrete quality using PZT transducers. Smart Struct Syst 2010;6(7):851–66.
[42] Rashid MA, Mansur MA, Paramasivam P. Behavior of aramid fiber-reinforced polymer reinforced high strength concrete beams under bending. J Compos Constr 2005;9(2):17–127.
[43] Khalifa A, Nanni A. Improving shear capacity of existing RC T-section beams using CFRP composites. Cem Concr Compos 2000;22(3):165–74.
[44] Trapko T. The effect of high temperature on the performance of CFRP and FRCM confined concrete elements. Compos Part B-Eng 2013;54:138–45.
[45] Lee HK, Simunovic S. A damage mechanics model of crack-weakened, chopped fiber composites under impact loading. Compos Part B-Eng 2002;33(1):25–34.
[46] Zhang C, Wang J. Interface stress redistribution in FRP-strengthened reinforced concrete beams using a three-parameter viscoelastic foundation model. Compos Part B-Eng 2012;43(8):3009–19.